

Needle detection in curvilinear ultrasound images based on the reflection pattern of circular ultrasound waves

Mohammad I. Daoud^{a)}

Department of Computer Engineering, German Jordanian University, Amman 11180, Jordan

Robert N. Rohling,^{a)} Septimiu E. Salcudean,^{a)} and Purang Abolmaesumi^{a)}

Department of Electrical and Computer Engineering, University of British Columbia, Vancouver, British Columbia V6T 1Z4, Canada

(Received 2 May 2015; revised 3 August 2015; accepted for publication 31 August 2015; published 8 October 2015)

Purpose: Ultrasound imaging provides a low-cost, real-time modality to guide needle insertion procedures, but localizing the needle using conventional ultrasound images is often challenging. Estimating the needle trajectory can increase the success rate of ultrasound-guided needle interventions and improve patient comfort. In this study, a novel method is introduced to localize the needle trajectory in curvilinear ultrasound images based on the needle reflection pattern of circular ultrasound waves.

Methods: A circular ultrasound wave was synthesized by sequentially firing the elements of a curvilinear transducer and recording the radio-frequency signals received by each element. Two features, namely, the large amplitude and repetitive reflection pattern, were used to identify the needle echoes in the received signals. The trajectory of the needle was estimated by fitting the arrival times of needle echoes to an equation that describes needle reflection of circular waves. The method was employed to estimate the trajectories of needles inserted in agar phantom, beef muscle, and porcine tissue specimens.

Results: The maximum error rates of estimating the needle trajectories were on the order of 1 mm and 3° for the radial and azimuth coordinates, respectively.

Conclusions: These results suggest that the proposed method can improve the robustness and accuracy of needle segmentation methods by adding signature-based detection of the needle trajectory in curvilinear ultrasound images. The method can be implemented on conventional ultrasound imaging systems. © 2015 American Association of Physicists in Medicine. [<http://dx.doi.org/10.1118/1.4932214>]

Key words: ultrasound imaging, needle detection, ultrasound-guided interventions, acoustic propagation and reflection

1. INTRODUCTION

Many minimally invasive procedures require inserting a needle toward a target location inside the human body. These interventions, although minimally invasive, involve safety and failure risks due to needle misplacement. Moreover, incorrect needle insertion might require needle redirections or repeated insertion attempts, which cause patient pain and discomfort.

Ultrasound imaging can improve the safety and success of the intervention by visualizing both the relevant anatomy and the advancing needle in real time. Ultrasound has a long history of guiding needle insertion procedures including biopsies^{1,2} and anesthesia.^{3,4} Generally, accurate visualization of patient anatomy using ultrasound can be achieved by employing experienced and trained operators. However, needle localization in both linear and curvilinear ultrasound images remains a challenging task due to several artifacts that degrade the appearance of the needle in ultrasound images.⁵ Examples of these artifacts are reverberation that is caused by ultrasound reflections within the needle shaft, the comet tail that appears below the needle, the side lobe artifact, and poor needle visibility at steep insertion angles due to needle echoes reflecting

away from the transducer.⁶ The reader is directed to the study by Huang *et al.*⁷ for detailed description of these artifacts. Traditionally, the physician approximates the needle position based on the observable portion of the needle and the motion of the tissue surrounding the needle during insertion.

Previous methods to improve needle visibility in ultrasound images can be broadly classified into three groups: image-based needle segmentation, external needle tracking systems, and imaging the needle using customized ultrasound excitation to maximize the echoes received from the needle. Many needle segmentation algorithms were focused on detecting the needle in two-dimensional (2D) ultrasound images. For example, Draper *et al.*⁸ developed an algorithm that combined image thresholding, binary closing, and component analysis to segment the needle in ultrasound images and present its position to the user. Ding and Fenster⁹ introduced a real-time 2D needle segmentation algorithm that employed a low-complexity Hough transform. Okazawa *et al.*¹⁰ proposed a real-time algorithm to segment curved needles in ultrasound images using a Hough transform with a modified coordinate transformation. A temporal-based algorithm was introduced by Cool *et al.*¹¹ to detect a prostate biopsy core in a series of

real-time ultrasound images. In this algorithm, the points of needle insertion and withdrawal were identified using temporal analysis and the biopsy core was determined by employing a Hough transform combined with temporo-spectral analysis.

Recent studies aimed at segmenting the needle in three-dimensional (3D) ultrasound images. For example, Novotny *et al.*¹² employed a generalized Radon transform implemented on a graphics processor unit (GPU) to track a long straight instrument in real-time 3D ultrasound images. The tip and roll angle of the instrument were identified by attaching passive markers to the shaft of the instrument. Uhercik *et al.*¹³ proposed a method to localize a thin surgical tool in 3D ultrasound images by thresholding the image to select the voxels with high intensity and performing random sample consensus (RANSAC) analysis to estimate the axis of the tool. Aboofazeli *et al.*¹⁴ developed a method for outlining curved needles in 3D ultrasound images by projecting the 3D image into a 2D image and segmenting the needle in the projected image. In the method proposed by Ding *et al.*,¹⁵ the needle trajectory was estimated in the 3D image by employing real-time volume rendering to generate two orthogonal 2D image projections and segmenting the generated 2D images. In general, 3D ultrasound is less widely used in minimally invasive procedures compared to 2D ultrasound due to the longer acquisition time and the challenge of interpreting 3D images.

External needle tracking was employed by the SonixGPS system (Ultrasonix, Inc., Richmond, BC, Canada),¹⁶ which estimates the 3D needle position with respect to the ultrasound image using an electromagnetic positioning system. Mung *et al.*¹⁷ proposed the use of small ultrasound sensors attached to the surgical tool. The sensors detect the signals transmitted by the imaging probe during 3D ultrasound-guided procedures. The detected signals are analyzed to estimate the 3D positions of the sensors, and hence localize the surgical tool. This technique has been extended in Ref. 18 to enable needle tracking using 2D ultrasound and employ low-cost copolymer and PZT ultrasound sensors. Stolka *et al.*¹⁹ proposed a camera-based needle tracking system, in which stereo cameras were mounted on the ultrasound probe to estimate the needle position and track the needle tip. Another technique to determine the needle position is to attach a piezoelectric actuator to the needle tip.²⁰ The actuator creates low-frequency vibrations, which are detected using color Doppler imaging to determine the needle position. Greer *et al.*²¹ combined B-mode and power Doppler ultrasound to segment curved needles in real time. External vibrations were used to excite the needle and induce Doppler response. The needle was reconstructed by analyzing pairs of B-mode and Doppler ultrasound images. The use of external needle tracking systems often involves additional costs and requires modified workflows, which might limit their application in clinical procedures.

One effective approach for improving needle visibility is to employ a specific ultrasound excitation pattern that maximizes the signals received from the needle without the use of external tracking systems or altering the clinical workflow. This approach has been used by Cheung and Rohling²² that introduced an adaptive beam steering algorithm to

continuously steer the ultrasound beam to an angle orthogonal to the needle. The adaptive beam steering provides an efficient technique for improving needle visibility using linear ultrasound transducers, but it has not been demonstrated for curvilinear transducers.

Curvilinear 2D ultrasound transducers are commonly used in needle insertion interventions due to their wide field of view compared to linear transducers.²³ Moreover, for clinically relevant needle insertion angles, curvilinear ultrasound transducers achieve better needle visibility compared to linear transducers since the probability of achieving orthogonal interception between the ultrasound beam and the needle is higher using curvilinear transducers.²³ One limitation in curvilinear transducers, which might affect the visibility of the needle, is the spacing between the scan lines that increases as a function of penetration depth. In general, curvilinear transducers are more ideally suited for needle interventions that involve deep structures, while linear transducers are usually preferred for procedures that involve superficial targets.^{24,25} Due to the wide use of curvilinear transducers in various needle insertion procedures, it is important to develop efficient methods for localizing the needle in curvilinear ultrasound images. This study aims to investigate the hypothesis that customized excitation of curvilinear 2D ultrasound transducers can be used to improve needle localization. In particular, we hypothesize that the needle reflection pattern of circular ultrasound waves and specific characteristics of needle echoes can be employed to estimate the needle trajectory in curvilinear ultrasound images. When a circular wave is transmitted to a needle surrounded with soft tissue, the arrival times of the echoes reflected from the needle depend on the coordinates of the needle axis. Moreover, the needle echoes are characterized by two needle-specific features, namely, the large amplitude and periodic reflection pattern. Hence, the needle trajectory can be estimated by transmitting a circular ultrasound wave and analyzing the received prebeamformed radio-frequency (RF) signals to determine the arrival times of needle echoes. In this study, the transmission of a circular ultrasound wave was achieved by sequentially actuating the elements of a curvilinear transducer. The recording of the prebeamformed RF signals was performed by employing custom parallel receive hardware that records the signals received by the individual elements. To evaluate the accuracy of the proposed needle localization method, the method was used to estimate the axis coordinates of a needle embedded in an agar phantom, a needle inserted in beef muscle, and four needles inserted in porcine tissue specimens. The proposed method has the potential to improve the robustness of needle localization methods, such as needle segmentation algorithms, by enabling a signature-based approach for detecting the needle trajectory in curvilinear ultrasound images, which can be incorporated with other needle detection features. A preliminary version of this work has appeared in Ref. 26 which provides a brief introduction to the needle reflection pattern of circular ultrasound waves and a limited phantom study.

The remainder of the paper is organized as follows. Section 2 describes the needle reflection pattern of circular waves and the two features used to identify needle echoes.

Moreover, Sec. 2 presents the method proposed to estimate the needle trajectory. The experiments performed to evaluate the accuracy of the proposed method are described in Sec. 3. Section 4 presents the results. Finally, the discussion and conclusion are provided in Secs. 5 and 6, respectively.

2. METHODS

The proposed method for localizing the needle is based on two components: the needle reflection pattern of circular ultrasound waves and the specific features that characterize needle echoes. In this section, these two components are investigated and then combined to enable accurate localization of the needle trajectory. The needle reflection pattern of circular ultrasound waves is analyzed in Subsection 2.A to relate the arrival times of needle echoes to the coordinates of the needle axis. In Subsection 2.B, the echoes reflected from two needle types at various ultrasound imaging configurations are analyzed to investigate specific features that can be used to identify needle echoes. Finally, the needle reflection pattern of circular ultrasound waves and the needle-specific features are combined in Subsection 2.C to estimate the axis coordinates of a needle embedded in soft tissue.

2.A. Needle reflection pattern of circular ultrasound waves

When a circular wave encounters a needle embedded in soft tissue, the metal surface of the needle acts as a planar reflector. In particular, the signal reflected by the needle matches a wave transmitted by a virtual point source placed behind the needle with the same orthogonal spacing between the needle surface and the source of the incident circular wave. This reflection pattern can be used to compute the theoretical arrival times of the needle echoes for a given needle position.

Consider an incident circular wave that is synthesized by sequentially actuating the elements of a curvilinear transducer. The equivalent point source of the incident circular wave is the center of curvature of the transducer. This imaging geometry is illustrated in Fig. 1 in which a curvilinear transducer is used

to transmit a circular wave to a tissue volume that includes a needle. The polar system, (r, α) , is used in the analysis, where r and α are the radial and azimuth coordinates, respectively. The azimuth dimension, α , is defined as the counterclockwise angle with respect to the curvilinear transducer central axis. The origin, $(0,0)$, of the coordinate system is located at the center of curvature of the transducer. The coordinates of the needle axis can be described using the line $\alpha = \phi$ that extends from the origin and orthogonally intersects with the needle at point (D, ϕ) , where D is the sum of the radius of curvature, R , of the transducer and the orthogonal spacing, A , between the surface of the transducer and the needle. In this paper, the angle ϕ is called the needle angle. The virtual point source of the signal reflected from the needle is located at point $(2D, \phi)$.

Assume that a transducer element is located at (R, θ) and let L denote the spacing between the virtual point source and that element. The value of L can be computed using the cosine law,

$$L = \sqrt{R^2 + (2D)^2 - 2R(2D)\cos(\phi - \theta)}, \quad (1)$$

where $D = R + A$.

The round-trip distance that the ultrasound wave propagates between the transducer element located at (R, θ) and the needle is equal to the difference between the spacing, L , and the radius of the transducer, R . Therefore, the theoretical arrival time, t , of the echo reflected from the needle and received by the element located at (R, θ) can be written as

$$t = \frac{\sqrt{R^2 + (2D)^2 - 2R(2D)\cos(\phi - \theta)} - R}{c}, \quad (2)$$

where c is the sound speed of the tissue between the needle and the transducer.

Equation (2) indicates that for a given transducer element located at (R, θ) , the arrival time of the needle echo depends on the coordinates D and ϕ that describe the needle axis.

2.B. Analyzing the characteristics of needle echoes

The metal, cylindrical structure of the needle is different from the surrounding tissue, and hence it is hypothesized that the echoes reflected from the needle possess needle-specific characteristics. In particular, ultrasound reflection at the interface between the needle surface and the tissue leads to echoes with large amplitude. Moreover, the ultrasound signals that penetrate inside the needle shaft will propagate backward and forward between the two metal needle walls.²⁷ Such needle-specific characteristics can be used to identify the needle echoes and estimate their experimental arrival times.

To evaluate this hypothesis, a Sonix MDP system (Ultra-sonix, Inc., Richmond, BC, Canada) was used to image two needles: a brachytherapy needle and a G17 needle. Ultrasound imaging of the needles was performed using the 4DC7-3/40 and MC9-4/12 curvilinear transducers, where each transducer included 128 piezoelectric elements. The 4DC7-3/40 transducer has a center frequency of 5.0 MHz, -6-dB bandwidth of 3 MHz, radius of curvature, R , of 39.0 mm, azimuth element spacing of 0.625° , and aperture angle, ψ , of 40° . The MC9-4/12 transducer has a center frequency of 6.0 MHz, -6-dB

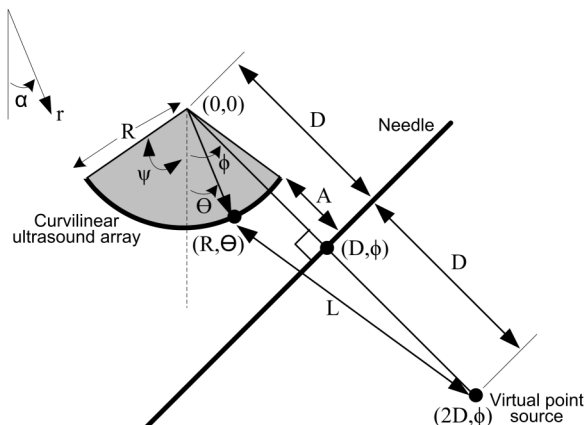


FIG. 1. The needle reflection pattern of a circular ultrasound wave transmitted by a curvilinear transducer.

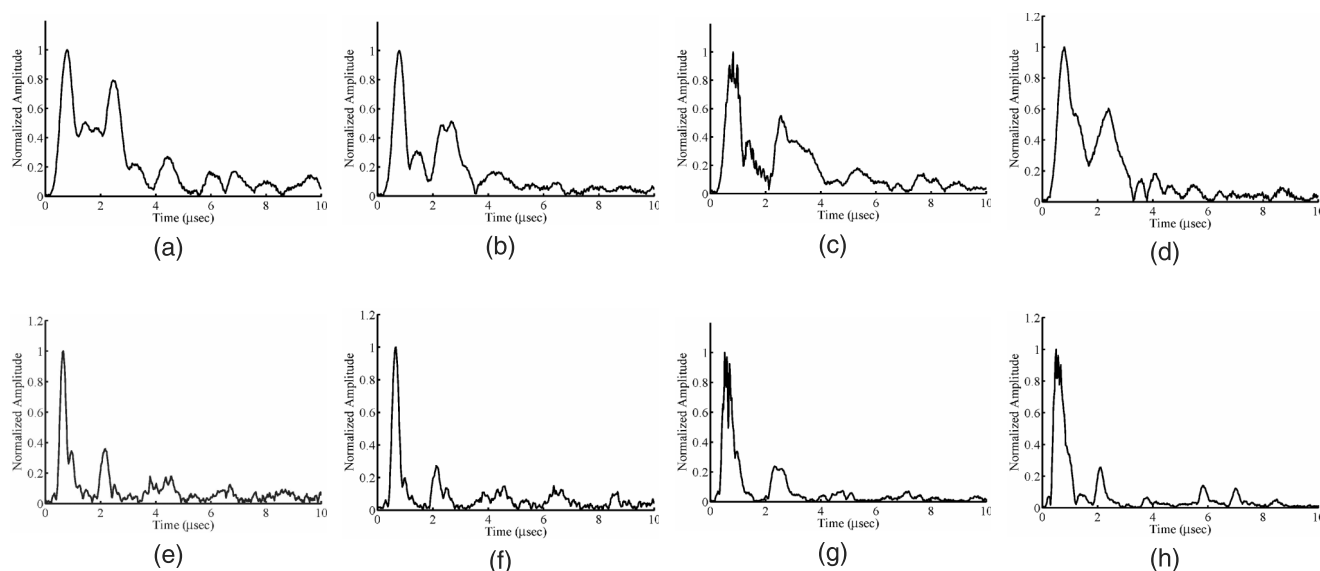


FIG. 2. (a)–(d) The envelopes of needle echoes recorded by the center element of the 4DC7-3/40 transducer during the imaging of (a) brachytherapy needle filled with water, (b) brachytherapy needle filled with air, (c) G17 needle filled with water, (d) G17 needle filled with air. (e)–(h) The envelopes of needle echoes recorded by the center element of the MC9-4/12 transducer during the imaging of (e) brachytherapy needle filled water, (f) brachytherapy needle filled with air, (g) G17 needle filled with water, (h) G17 needle filled with air.

bandwidth of 3.6 MHz, radius of curvature of 12.5 mm, azimuth element spacing of 1.05° , and aperture angle of 67° . The imaging system employed custom parallel receive hardware (Sonix DAQ, Ultrasonix, Inc.) that records the prebeamformed RF signals received by the individual elements. Each prebeamformed RF signal was recorded for $100\ \mu\text{s}$ and sampled using an analog-to-digital converter with a sampling frequency of 40 MHz.

In the first needle imaging test, the 4DC7-3/40 transducer was employed to image a brachytherapy needle that was filled and embedded in water. During imaging, the needle angle, ϕ , was approximately set to 0° . The imaging system was configured to approximate a single circular incident wave by sequentially firing the transducer elements and recording the prebeamformed RF signals received by all elements during each individual-element actuation. The firing rate was set to match the rate of B-mode image formulation with a depth of 8 cm. For each element, an ensemble RF signal was synthesized by coherently adding the prebeamformed RF signals received by this element during the 128 individual-element actuations. This ensemble RF signal approximates the signal received by the element when a circular wave is transmitted. The process of transmitting a circular wave and computing the ensemble RF signals was repeated for five trials.

To evaluate the effect of changing the material inside the needle on the needle echoes, the five-trial ultrasound imaging of the brachytherapy needle was repeated when the needle was filled with air and surrounded with water. Moreover, the influence of altering the type of the needle was investigated by imaging a G17 needle that was embedded in water and separately filled with water and air. In addition, the effect of changing the ultrasound transducer was evaluated by using the MC9-4/12 transducer to carry out the five-trial ultrasound imaging of the brachytherapy needle and the G17 needle when each needle was separately filled with water and air.

For each of the eight combinations of transducer type, needle type, and material inside the needle, the envelope of a needle echo received by the center transducer element is shown in Fig. 2. The envelopes of needle echoes are characterized by large amplitude and repetitive reflection pattern. The large amplitude is attributed to wave reflection at the needle surface that produces echoes with high energy. The repetitive reflection pattern has a periodic interval on the order of $2\ \mu\text{s}$. In general, the peaks of the repetitive reflection pattern are decaying as a function of arrival time. The first three peaks are located within a $6\text{-}\mu\text{s}$ interval. It is worth noting that a similar periodic signature has been observed in the signals received from brachytherapy seeds.²⁸

The power spectral density (PSD) of each needle echo envelope presented in Fig. 2 was computed using the autoregressive spectral method.²⁹ The computation of the PSD was limited to the $6\text{-}\mu\text{s}$ segment that includes the first three peaks of the repetitive reflection pattern. The $6\text{-}\mu\text{s}$ segment was multiplied by a Hann window of similar length to reduce Gibbs phenomenon due to time-domain truncation. The PSDs are shown in Fig. 3. All PSDs include resonant peaks decaying as a function of frequency, which correspond to the repetitive reflection pattern that appears in the needle echo envelopes.

The PSDs of the recorded needle echoes have been analyzed to quantify the fundamental frequency of the repetitive reflection pattern. The analysis was limited to the transducer elements that received the strongest needle echoes. To identify these elements, the RF signals received by the individual transducer elements during each of the needle imaging trials were processed to extract the $6\text{-}\mu\text{s}$ segments that include the first three peaks of the needle echo. The energy of the envelope of each extracted segment was computed. In all imaging trials, it has been observed that the element located at the needle angle, ϕ , received the needle echo with the highest energy. Moreover, the energy of needle echoes received by the other

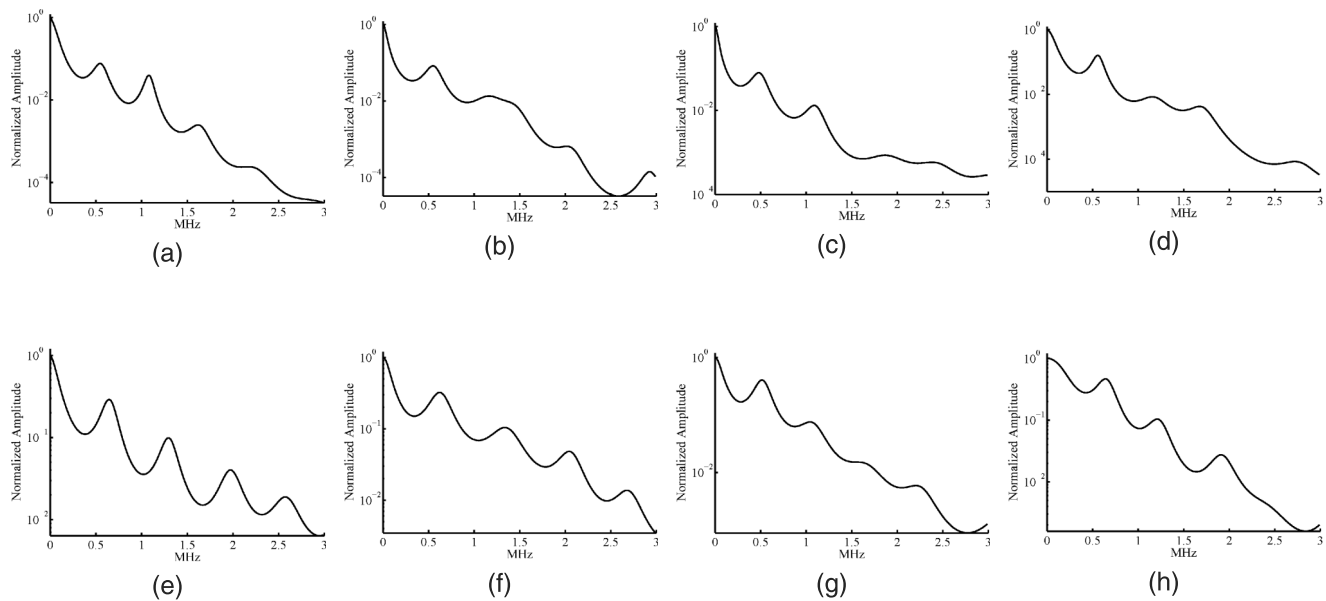


FIG. 3. (a)–(d) The PSD of needle echoes recorded by the center element of the 4DC7-3/40 transducer during the imaging of (a) brachytherapy needle filled with water, (b) brachytherapy needle filled with air, (c) G17 needle filled with water, (d) G17 needle filled with air. (e)–(h) The PSD of needle echoes recorded by the center element of the MC9-4/12 transducer during the imaging of (e) brachytherapy needle filled water, (f) brachytherapy needle filled with air, (g) G17 needle filled with water, (h) G17 needle filled with air.

elements decreased as a function of the difference between the azimuth angle of the receiving element and ϕ . In particular, for the 4DC7-3/40 and MC9-4/12 transducers, the energy of the needle echo drops below 10% of the maximum needle echo energy, which is received by the element located at ϕ , when the difference between the azimuth angle of the receiving element and ϕ exceeded 20° and 22° , respectively. This decrease in energy is attributed to the directivity of the element and the increase in propagation path of the received needle echo. Based on this analysis, an active receive aperture has been defined for the 4DC7-3/40 transducer such that it is composed of the 65 adjacent elements that are located within an azimuth range of 20° with respect to ϕ . Similarly, an active receive aperture was defined for the MC9-4/12 transducer such that it is composed of the 43 adjacent elements that are located within an azimuth range of 22° with respect to ϕ . It is worth noting that a practical criterion to identify the elements in the active receive aperture is described in Subsection 2.C.

The spectra of the needle echoes received by the elements in the active receive aperture during the five imaging trials carried out for each combination of ultrasound transducer, needle type, and material inside the needle were analyzed. The analysis was performed by extracting the 6- μ s segment that includes the first three peaks of the needle echo from each RF signal and computing the PSD as described above. For each combination, the mean \pm standard deviation of the spacing between the largest and second largest peaks, Δf_1 , of the PSDs computed for the five imaging trials are shown in Table I. Moreover, the mean \pm standard deviation of the spacing between the second and third largest peaks, Δf_2 , of the PSDs computed for each combination are shown in the table. For all combinations examined in this study, the values of Δf_1 and Δf_2 are mainly between 0.40 and 0.75 MHz. It is worth noting that the number of needle echoes employed to compute Δf_1 and Δf_2 for each

combination is equal to the number of elements in the active receive aperture, i.e., 65 and 43 for the 4DC7-3/40 and MC9-4/12 transducers, respectively, multiplied by five (the number imaging trial per combination).

The analysis presented in this subsection suggests that the needle echoes can be identified based on two needle-specific features: the large amplitude and the periodic reflection pattern.

2.C. Computing the coordinates of the needle axis

The needle reflection pattern of circular ultrasound waves and the needle-specific features, which were discussed in Subsections 2.A and 2.B, respectively, were used to estimate the axis coordinates of the needle as described in Fig. 4. In particular, a circular ultrasound wave was transmitted to the needle and the RF signals received by the elements in the

TABLE I. The mean \pm standard deviation of the spacings between the largest and second largest peaks, Δf_1 , and the second largest and third largest peaks, Δf_2 , of the PSDs computed for the five imaging trials performed for each combination of ultrasound transducer, needle type, and material inside the needle.

Transducer	Needle	Needle filling	Δf_1 (MHz)	Δf_2 (MHz)
4DC7-3/40	Brachytherapy	Water	0.49 ± 0.09	0.60 ± 0.10
4DC7-3/40	Brachytherapy	Air	0.50 ± 0.08	0.61 ± 0.09
4DC7-3/40	G17	Water	0.51 ± 0.10	0.64 ± 0.11
4DC7-3/40	G17	Air	0.53 ± 0.09	0.59 ± 0.10
MC9-4/12	Brachytherapy	Water	0.59 ± 0.09	0.67 ± 0.09
MC9-4/12	Brachytherapy	Air	0.62 ± 0.07	0.69 ± 0.08
MC9-4/12	G17	Water	0.48 ± 0.04	0.54 ± 0.05
MC9-4/12	G17	Air	0.62 ± 0.06	0.61 ± 0.05

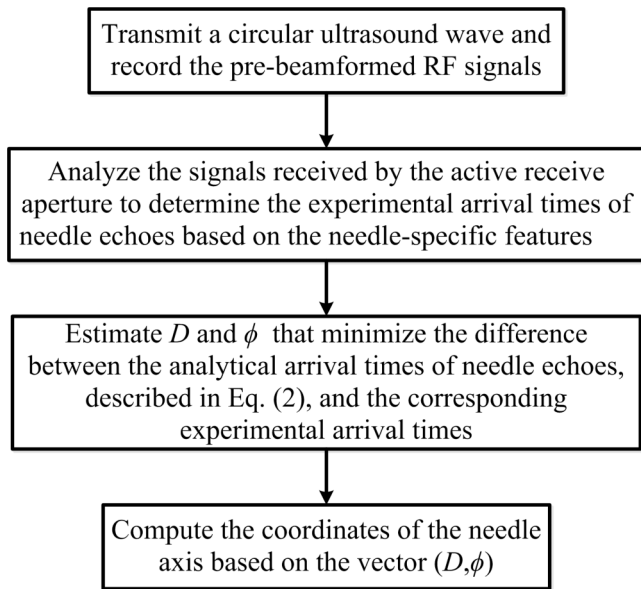


FIG. 4. A flowchart that summarizes the procedure used to estimate the axis coordinates of a needle embedded in soft tissue based on the needle reflection pattern of circular ultrasound waves and the needle-specific features.

active receive aperture were analyzed using the large amplitude and periodic reflection pattern features to determine the experimental arrival times of needle echoes. The vector (D, ϕ) , which describes the coordinates of the needle axis, was fitted to Eq. (2) to minimize the difference between the theoretical arrival times of the needle echoes computed using the equation and the matching experimental arrival times. The computation of the needle axis coordinates was limited to the elements in the active receive aperture since the acoustic energy reflected by the needle is mainly received by these elements, as discussed in Subsection 2.B.

The experimental arrival time of the needle echo received by a particular transducer element was determined by searching the ensemble RF signal received by that element sequentially starting from the region near the transducer surface. The analysis presented in Subsection 2.B indicates that the first three peaks of the repetitive needle reflection pattern are included within a $6\text{-}\mu\text{s}$ interval. Therefore, the quantification of the two needle-specific features was performed by applying a sliding window to the RF signal to extract a $6\text{-}\mu\text{s}$ segment. The segment was then analyzed, as described below, to determine if it includes the large amplitude and the periodic reflection pattern features. If the segment was found to include these two features, then the search was terminated and the arrival time of the needle echo was assumed to correspond to the RF sample with the greatest amplitude in the segment. Otherwise, the search continued by iteratively shifting the sliding window away from the transducer by $0.1\text{ }\mu\text{s}$ to extract another segment and determine if it includes the first three peaks of the needle echo. If the entire RF signal was searched without finding the needle echo, then the element that received the RF signal was excluded from the computation of the needle axis coordinates.

As discussed in Subsection 2.B, if the extracted segment includes the first three peaks of the needle echo, then the strongest peak is expected to be located within the first third of

the segment. Since the needle echo is essentially generated by specular reflection at the needle surface, then the amplitude of the strongest peak of the needle echo is expected to be multiple times greater than the mean amplitude value of the entire RF signal, which is usually dominated by tissue backscattered signals. Therefore, a simple and effective criterion can be used to quantify the large amplitude feature by comparing the RF samples in the first third of the segment with the mean envelope of the entire RF signal. In particular, if 50% of the RF samples in the first third of the segment have values greater than three times the mean envelope of the entire RF signal, then the segment is considered to satisfy the large amplitude feature.

To quantify the repetitive reflection pattern feature, the spectral analysis of needle echoes, presented in Subsection 2.B, was considered. This analysis suggests that the PSD of the $6\text{-}\mu\text{s}$ segment that includes the first three peaks of the needle echoes received from the brachytherapy and G17 needles has resonant peaks, where the spacings between the largest and second largest peaks, Δf_1 , and the second and third largest peaks, Δf_2 , are between 0.40 and 0.75 MHz. Therefore, the computation of the repetitive reflection pattern feature was performed by calculating the PSD of the extracted segment using the autoregressive spectral method²⁹ and measuring the values of Δf_1 and Δf_2 . If the values of Δf_1 and Δf_2 are between 0.40 and 0.75 MHz, then the segment is considered to satisfy the repetitive reflection pattern feature.

Exact selection of the elements in the active receive aperture is infeasible because the coordinates of the needle are unknown. In this study, the active receive apertures of the 4DC7-3/40 and MC9-4/12 transducers were initially approximated by asking the user to manually select a subset of 65 and 43 adjacent elements, respectively, that form a central axis orthogonal to the needle. This initial estimation of the needle axis was performed based on the visible portion of the needle. The ensemble RF signals received by the manually selected elements were analyzed, as described above, to detect the echoes reflected by the needle. The active receive aperture was then readjusted such that its center is as close as possible to the element that received the strongest needle echo.

The N elements in the active receive aperture were numbered sequentially between 1 and N . The experimental arrival times of needle echoes estimated for the elements in the active receive aperture based on the RF signals were represented as the set $\hat{T} = \{\hat{t}_1, \hat{t}_2, \dots, \hat{t}_N\}$, where \hat{t}_i is the arrival time of the needle echo received by the i th element. The matching analytical values of the arrival times, computed using Eq. (2), were represented using the set $T = \{t_1, t_2, \dots, t_N\}$, where t_i denotes the arrival time of the needle echo received by the i th element. The value of t_i depends on the radius of curvature of the transducer, R , the azimuth angle of the i th element, θ_i , the sound speed, c , of the tissue between the needle and the transducer, and the values of D and ϕ that describe the coordinates of the needle axis.

The coordinates of the needle axis were estimated by performing unconstrained nonlinear regression of the values of D and ϕ to minimize the sum-of-squared errors between the analytical arrival times of needle echoes, T ,

and the experimental arrival times of the needle echoes, \hat{T} . The unconstrained nonlinear regression was carried out using the MATLAB (The MathWorks, Inc., Natick, MA) function, *fminsearch*, which employs the simplex search method of Lagarias.³⁰ In this study, the values of the coordinates D and ϕ estimated using the proposed ultrasound signature-based method are called D_{US} and ϕ_{US} , respectively.

3. EXPERIMENTS

In this section, the accuracy of estimating of the needle axis coordinates based on the needle reflection pattern of circular ultrasound waves was evaluated by computing the axis coordinates of needles embedded in agar phantom, beef muscle, and porcine tissue specimens. The ultrasonically estimated axis coordinates of the needles were compared with ground truth coordinates obtained using 3D CT imaging. Moreover, the values of Δf_1 and Δf_2 were computed for the real tissue specimens, i.e., beef muscle and porcine tissue specimens, and compared with the values reported in Subsection 2.B.

3.A. Ultrasound imaging setup

Ultrasound imaging was performed using the Sonix MDP system and the 4DC7-3/40 and MC9-4/12 transducers. The DAQ parallel receive hardware was used to record the pre-beamformed RF signals of the individual elements. At each ultrasound acquisition, the transducer was fixed and oriented such that the needle being imaged was included in the imaging plane as shown in Fig. 1. The imaging system was configured as described in Subsection 2.B to approximate an incident circular wave and synthesize the ensemble RF signals of the individual elements.

The prebeamformed RF signals acquired at each acquisition were processed to construct a B-mode image using the multielement synthetic aperture focusing (MSAF) technique³¹ that is summarized in the Appendix. Moreover, the imaging system was configured to acquire a conventional B-mode image with fixed focus, such that the needle is included in the focal zone. The B-mode image obtained using the MSAF technique was spatially compounded with the fixed-focus B-mode image.

3.B. Agar phantom experiment

The 4DC7-3/40 transducer was used to image a brachytherapy needle with a diameter of 1.25 mm embedded in agar phantom. The phantom included a nylon wire that was placed 26 mm below the needle, parallel to the needle axis. Moreover, the phantom included four nylon wires with interwire spacing of ~ 20 mm that were placed ~ 15 mm below the needle and orthogonal to the plane that includes the axis of the needle and the wire parallel to the needle. The transducer was oriented such that the imaging plane included both the needle and the nylon wire parallel to the needle. The four wires orthogonal to the imaging plane were used as fiducial markers. The transducer was rotated using the mechanical manipulator to

vary the needle angle, ϕ , between 0° and the aperture angle of the transducer (40°) with 5° increments. The value of the needle angle measured manually based on the orientation of the ultrasound transducer was denoted as ϕ_{man} . At each transducer orientation, the ultrasound data were acquired.

3.C. Beef tissue experiment

In vitro evaluation of the proposed method was performed by employing the 4DC7-3/40 transducer to image a brachytherapy needle with a diameter of 1.25 mm inserted in a fresh store-bought beef muscle specimen. A metal needle stylet was placed ~ 21 mm below the needle in a direction parallel to the needle axis. Five parallel wood rods with a diameter of 2.5 mm and inter-rod spacing of ~ 20 mm were inserted ~ 27 mm below the needle in a direction orthogonal to the plane that includes the axes of the needle and the metal stylet. These wood rods were used as fiducial markers. The transducer was oriented such that the imaging plane includes both the needle and the stylet. The transducer was rotated using the mechanical manipulator to vary the needle angle, ϕ_{man} , between 0° and the aperture angle of the transducer with 5° increments. The ultrasound data were collected at each transducer orientation.

3.D. Porcine tissue experiment

The MC9-4/12 transducer was used to image four G17 needles with a diameter of 1.5 mm inserted into the epidural space of two fresh store-bought porcine tissue specimens obtained from the back of the animal. Each needle was inserted into the epidural space such that the sagittal and transverse angles of the needle were within the range of angles reported in a previous clinical epidural study.³² The sagittal and transverse angles of the four needles are presented in Table II. For each needle, a 1-mm metal stylet was inserted ~ 10 mm below the needle, parallel to the needle axis. The spacing between each needle and its parallel stylet was fixed by guiding the needle and the stylet during their insertion into the porcine tissue using a custom-made guide. For each needle, two parallel 3-mm metal stylets separated by ~ 10 mm were inserted such that the first stylet was located between 1.1 and 1.7 mm above the needle and the second stylet was positioned between 2.2 and 2.8 mm above the needle in a direction orthogonal to the plane that includes both the needle and the stylet parallel to the needle. The two 3-mm stylets were used as fiducial markers. The MC9-4/12 transducer was used to separately image each needle. Before imaging, the skin and fat layers located at the surface of the porcine tissue specimen were removed. The

TABLE II. The sagittal and transverse angles of the four G17 needles inserted into the porcine tissue specimens.

Needle number	Sagittal angle (deg)	Transverse angle (deg)
1	15	26
2	19	44
3	20	29
4	23	39

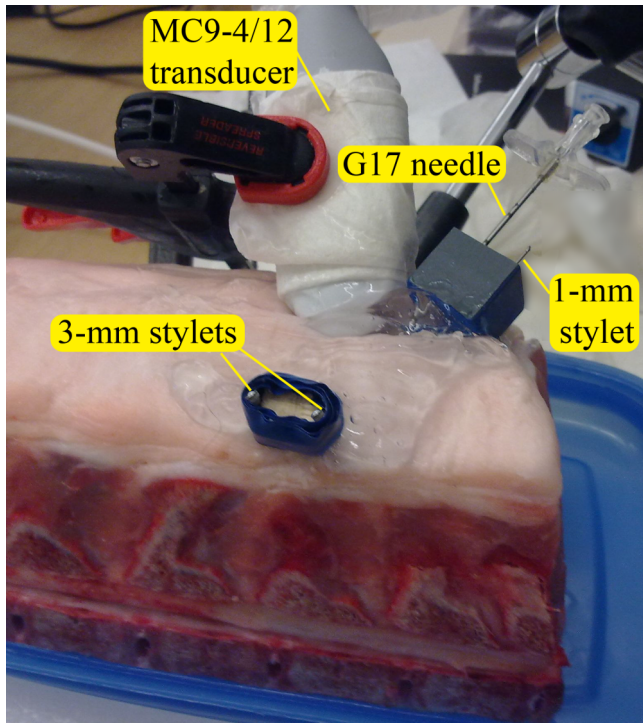


FIG. 5. The setup used to image a needle inserted in a porcine tissue specimen.

transducer was positioned using the mechanical manipulator such that the needle and the stylet parallel to the needle were included in the imaging plane. Moreover, the needle angle, ϕ_{man} , was set to a value between 50° and the aperture angle of the transducer (67°). Ultrasound imaging was then performed to acquire the data. Figure 5 illustrates the imaging setup used to image the needles inserted in the porcine tissue specimens.

3.E. Accuracy analysis

The accuracy of localizing the needle embedded in the agar phantom was evaluated by comparing the needle axis coordinates, D_{US} and ϕ_{US} , computed using the proposed method with the matching coordinates obtained using a 3D CT image of the phantom. To register the ultrasound data to the 3D CT image, a spatially compounded B-mode image was synthesized for each transducer orientation employed for imaging by compounding the B-mode image obtained using the MSAF technique with the matching conventional fixed-focus B-mode image. Each spatially compounded B-mode image was registered manually to the 2D plane in 3D CT image that includes both the needle and the nylon wire parallel to the needle. Registration was performed by manually matching the fiducial markers in the B-mode image with the fiducial markers in the 2D CT image plane. The center of curvature of the transducer was taken as the intersection of the two radii of the B-mode image acquired at that orientation. Moreover, the central axis of the transducer was estimated by drawing a line along the radial dimension of the B-mode image such that the line divides the B-mode images into two equal sectors. The ground truth values of the coordinates D and ϕ were computed for each transducer

orientation by drawing a vector from the transducer center of curvature to the needle in the registered CT image plane such that the vector orthogonally intercepts with needle. The ground truth values of D and ϕ were denoted D_{GT} and ϕ_{GT} , respectively. The errors, ΔD and $\Delta\phi$, of estimating D and ϕ , respectively, using the proposed method were defined as

$$\Delta D = |D_{\text{GT}} - D_{\text{US}}|, \quad (3)$$

$$\Delta\phi = |\phi_{\text{GT}} - \phi_{\text{US}}|, \quad (4)$$

where $||$ represents the absolute value operator.

To evaluate if the values of Δf_1 and Δf_2 that are reported in Subsection 2.B can be applied for real tissue, the mean \pm standard deviation of these two quantities were computed for the needle inserted in the beef muscle for all transducer orientations employed for imaging. Moreover, the mean \pm standard deviation of Δf_1 and Δf_2 were reported for the four needles inserted in the porcine tissue specimens. The computation was limited to the needle echoes received by the elements in the active receive aperture.

The ground truth values of the needle axis coordinates, D_{GT} and ϕ_{GT} , and the errors ΔD and $\Delta\phi$ were computed for the needle inserted in the beef muscle and the four needles inserted in the porcine tissue specimens using the same technique that was employed for agar phantom. The only variation is that the spatially compounded B-mode image was registered to the plane in the CT image that includes the needle and the metal stylet parallel to the needle.

In all ultrasound data analyses, the sound speed in agar and beef muscle was set to 1540 m/s (Ref. 33) and 1547 m/s,³⁴ respectively. The sound speed in porcine tissue was assumed to be equal to pig muscle [1558 m/s (Ref. 35)].

4. RESULTS

4.A. Agar phantom results

The manually measured needle angle, ϕ_{Man} , and the ground truth axis coordinates, $(D_{\text{GT}}, \phi_{\text{GT}})$, of the needle embedded in agar phantom, as described in Subsection 3.B, are presented in Table III for each transducer orientation employed for

TABLE III. Accuracy of estimating the axis coordinates of the needle inserted in agar phantom using the needle reflection pattern of circular ultrasound waves.

ϕ_{Man} (deg)	Ground truth coordinates of the needle axis		Estimation error of the needle axis coordinates	
	D_{GT} (mm)	ϕ_{GT} (deg)	$ \Delta D $ (mm)	$ \Delta\phi $ (deg)
0	52.2	3.8	0.4	0.7
5	53.4	7.5	0.3	2.0
10	53.3	13.2	0.2	0.9
15	53.4	18.4	0.4	1.3
20	52.9	23.2	0.1	1.4
25	52.5	28.3	0.2	1.1
30	52.6	33.0	0.3	0.0
35	51.9	36.2	0.5	0.3
40	54.2	41.0	0.1	3.1

TABLE IV. Accuracy of estimating the axis coordinates of the needle inserted in beef muscle using the needle reflection pattern of circular ultrasound waves.

ϕ_{Man} (deg)	Ground truth coordinates of the needle axis		Estimation error of the needle axis coordinates	
	D_{GT} (mm)	ϕ_{GT} (deg)	$ \Delta D $ (mm)	$ \Delta \phi $ (deg)
0	61.5	-1.6	0.8	1.9
5	63.7	6.1	0.9	0.5
10	65.0	12.3	0.1	0.6
15	67.8	16.7	0.5	1.8
20	64.2	21.9	0.1	1.9
25	59.4	23.7	0.5	2.4
30	66.1	29.7	0.3	0.2
35	61.8	36.5	0.8	1.1
40	61.3	40.1	1.7	3.2

imaging. Furthermore, the errors, $(\Delta D, \Delta \phi)$, of estimating the needle axis coordinates at each transducer orientation using the needle reflection pattern of circular ultrasound waves are shown in the table. The error of estimating the radial coordinate, ΔD , of the needle is between 0.1 and 0.5 mm for all values of the needle angle, ϕ_{GT} , employed for imaging. The error of estimating the azimuth coordinate, $\Delta \phi$, of the needle is less than or equal to 2.0° when the needle angle, ϕ_{GT} , is smaller than the aperture angle of the 4DC7-3/40 transducer (40°). However, the value of $\Delta \phi$ increases to 3.1° when the needle angle, ϕ_{GT} , is close to the aperture angle of the transducer. The values of $(\Delta D, \Delta \phi)$ reported in Table III suggest that the needle axis coordinates can be estimated accurately based on the needle reflection pattern of circular ultrasound waves when the needle angle is less than or equal to the transducer aperture angle.

4.B. Beef tissue results

The mean \pm standard deviation of Δf_1 and Δf_2 computed for the needle inserted in the beef muscle specimen, as described in Subsection 3.C, for all transducer orientations employed for imaging are equal to 0.54 ± 0.24 and 0.65 ± 0.34 MHz, respectively. The axis coordinates of the needle and the errors of estimating the needle axis coordinates are presented in Table IV. When the needle angle, ϕ_{GT} , is smaller than the aperture angle of the 4DC7-3/40 transducer, the values of ΔD and $\Delta \phi$ are less than 1 mm and 2.5° , respectively. However, the values of ΔD and $\Delta \phi$ increase to 1.7 mm and 3.2° , respectively,

TABLE V. Accuracy of estimating the axes coordinates of the needles inserted in porcine tissue using the needle reflection pattern of circular ultrasound waves.

Needle number	Ground truth coordinates of the needle axis		Estimation error of the needle axis coordinates	
	D_{GT} (mm)	ϕ_{GT} (deg)	$ \Delta D $ (mm)	$ \Delta \phi $ (deg)
1	21.9	53.4	0.4	0.6
2	20.0	56.5	0.3	2.0
3	20.4	56.5	0.4	2.1
4	25.1	51.6	0.4	0.5

when ϕ_{GT} is close to the aperture angle of the transducer. Two spatially compounded B-mode images synthesized for the needle when the ground truth coordinates of the needle axis are equal to $(67.8 \text{ mm}, 16.7^\circ)$ and $(61.8 \text{ mm}, 36.5^\circ)$ are presented in Fig. 6. The needle axis estimated using the proposed method is shown as a white line.

4.C. Porcine tissue results

The spectral analysis of the echoes received from the four needles inserted in porcine tissue specimens indicated that Δf_1 and Δf_2 are equal to 0.50 ± 0.34 and 0.60 ± 0.41 MHz, respectively. The ground truth coordinates and error analysis obtained for the axes of the four needles are summarized in Table V. The azimuth coordinates, ϕ_{GT} , of the four needles are within the range of 51.6° – 56.5° . These values of needle angle are smaller than the aperture angle of the MC9-4/12 transducer (67°). The errors ΔD and $\Delta \phi$ are within the ranges of 0.3–0.4 mm and 0.5° – 2.1° , respectively. These results indicate that the proposed method has the potential to enable accurate needle localization during ultrasound-guided needle interventions. The spatially compounded B-mode images synthesized for the four needles are shown in Fig. 7.

5. DISCUSSION

The proposed needle detection method enables needle trajectory estimation without the use of external tracking systems or changing the clinical workflow of the intervention. The error of estimating the needle trajectory using the proposed method was evaluated by employing CT scan as a ground truth since it is completely independent of ultrasound

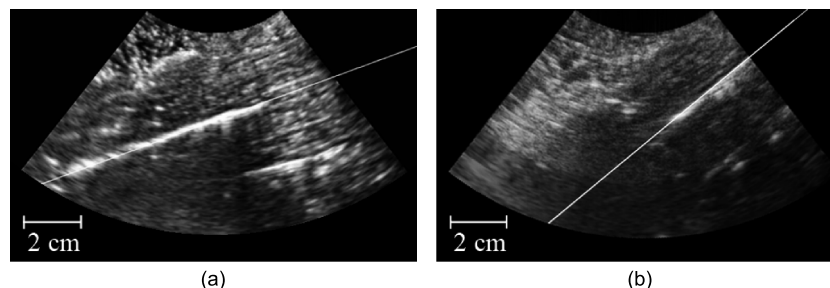


FIG. 6. B-mode images synthesized for the needle inserted in beef muscle when the ground truth coordinates of the needle axis are (a) $(67.8 \text{ mm}, 16.7^\circ)$ and (b) $(61.8 \text{ mm}, 36.5^\circ)$. Each image shows the axis of the needle estimated using the proposed method.

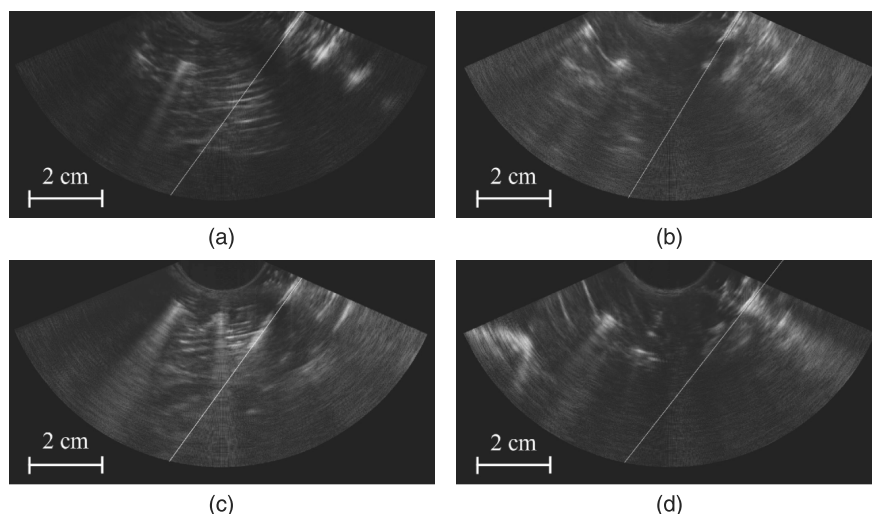


FIG. 7. The B-mode images synthesized for the four needles inserted in porcine tissue specimens. Each image shows the axis of the needle estimated using the proposed method. The sagittal and transverse angles of the needles are (a) 15° , 26° , (b) 19° , 44° , (c) 20° , 29° , and (d) 23° , 39° .

imaging (on average, the fiducial registration error between CT and ultrasound computed based on the point fiducial markers was on the order of 0.3 mm). The accuracy results obtained using the proposed method, which does not require the use of external tracking systems or changing the clinical workflow of the intervention, are comparable to the results achieved with advanced segmentation algorithms and dedicated needle tracking systems. In particular, the mean \pm standard deviation errors of estimating the radial and azimuth coordinates of the needle axis are 0.6 ± 0.5 mm and $1.5^\circ \pm 1.0^\circ$ in beef tissue and 0.4 ± 0.1 mm and $1.3^\circ \pm 0.9^\circ$ in porcine tissue. In comparison, the temporal-based needle segmentation algorithm, proposed by Cool *et al.*,¹¹ estimated the axes coordinates of biopsies needles during clinical prostate biopsy procedures with mean \pm standard deviation errors of 0.5 ± 0.4 mm (the orthogonal distance between the estimated and manually segmented needle axes measured at the needle tip) and $2.3^\circ \pm 2.0^\circ$ (the angular difference between the estimated and manually segmented needle axes). Furthermore, the SonixGPS system, which employs 3D electromagnetic position sensors, can enable needle tracking accuracy on the order of 2 mm.³⁶ The method presented by Mung *et al.*,¹⁷ in which small ultrasound sensors are mounted on the surgical tool, achieved 3D tracking error of 0.4 ± 0.2 mm. An important finding of the proposed method is the feasibility of estimating the needle trajectory using a signature-based approach. Such an approach can be combined with other methods for needle detection to improve the tracking robustness and accuracy.

One limitation in the proposed method is the localization of the needle tip. However, in several needle interventions, accurate localization of the needle tip based on ultrasound images is infeasible since the tip leaves the imaging plane during operator manipulation of the needle. Several clinical needles, such as epidural needles, include uniform markings on the shaft to estimate the insertion depth. Therefore, the needle tip can be localized by combining the estimation of needle trajectory, which is enabled using the proposed method, along with the insertion depth of the needle that is computed

based on the needle markings. In fact, the future direction of this study will be focused on evaluating the feasibility and accuracy of this approach for estimating the needle tip.

A requirement of the proposed needle localization method is the transmission of a circular wave. This requirement can be overcome by simultaneously firing the elements of a curvilinear transducer, which are distributed uniformly along a circular arc, to create a circular wavefront within the azimuth range covered by the aperture, i.e., $[-\psi, \psi]$. However, most ultrasound imaging systems have fewer transmit channels than the number of transducer elements. In particular, the Sonix MDP system does not support instantaneous excitation of the 128 elements of the 4DC7-3/40 and MC9-4/12 transducers. In this study, the circular wave was synthesized by sequentially firing each element and employing a custom parallel receive hardware to record the prebeamformed RF signals received by the individual elements during the 128 excitations. A drawback of using individual-element excitation is the small transmit aperture that reduces the penetration depth of needle detection. The penetration depth and signal to noise ratio (SNR) can be improved by employing multielement transmit aperture with defocusing phasing, as described in Ref. 31, to mimic individual-element excitation with high acoustic power. It is worth noting that the B-mode images synthesized using the MSAF technique based on the prebeamformed RF signals have small SNR. Therefore, each image obtained using the MSAF technique was spatially compounded with the matching fixed-focus B-mode image to improve the SNR.

As mentioned above, the synthesized circular waves were limited to the azimuth range $[-\psi, \psi]$, and hence it is important to consider the effect of the two ends of the transducer. The waves transmitted at the two ends of the transducer are expected to travel in directions that differ from the propagation path of the desired circular wave. Therefore, the interaction between these waves and the needle will interfere with the needle reflection pattern of the circular wave. To reduce the effect of the two ends of the transducer, the virtual point source, located at the azimuth angle ϕ that matches the needle angle,

was placed within the azimuth range of the circular wave by limiting the needle angle to values below or equal to the transducer aperture angle, ψ . Using this setup, the needle axis was detected in all phantom and *in vitro* needle experiments with maximum error rates on the order of 1 mm and 3° for the radial and azimuth coordinates of the needle axis. The results reported for the needle embedded in agar phantom and the needle inserted in beef muscle show a small increase in the estimation error of needle trajectory when the needle angle, ϕ , is close to ψ compared to the errors obtained using smaller needle angles. It has been noticed that increasing the needle angle, ϕ , to values greater than ψ leads to dramatic increase in the estimation error of needle trajectory.

A crucial part of the proposed method is the identification of the active receive aperture in each exam. The two-phase, semiautomated selection of the active receive aperture offers the advantages of high selection accuracy and low processing requirements. The first phase, which involves manual estimation of the active receive aperture based on the visible portion of the needle, aims to limit the search to an approximate set of elements located around the actual active receive aperture. The selected elements are searched in the second phase to determine the central element of the active receive aperture. The search is based on the fact that the strongest needle echo is received by the central element of the active receive aperture since the distance between the needle and the transducer is minimal at this element. Such a semiautomated selection minimizes the effect of human error and does not involve complex computational operations. Fully automatic selection of the elements in the active receive aperture can be achieved by replacing the manual selection phase with image and/or signal processing phase, in which a stream of B-mode ultrasound images or Doppler signals acquired during needle insertion and manipulation is analyzed using motion detection techniques to identify tissue motion in the region surrounding the needle. The elements that approximately cover this region are selected as active receive aperture. Similar to the approach employed in the present study, the approximate selection of the active receive aperture can be tuned in the second phase to improve the selection accuracy.

Another important process in the proposed method is the identification of the needle echoes to determine their experimental arrival times. Two features, namely, the large amplitude feature and the repetitive reflection pattern feature, have been used to accurately identify the needle echoes. The criterion used to quantify the large amplitude feature assumes that the first peak of the repetitive needle reflection pattern, which is expected to be located within the first third of the extracted 6- μ s segment, is multiple times greater than the average amplitude value of the entire RF signal. Such an assumption is satisfied if the RF signal is mainly dominated by tissue backscattered signals. However, if the RF signal includes echoes generated due to strong ultrasound reflections at structures other than the needle, such as bone, then an improved criterion should be employed. For example, the RF samples of the first third of the segment can be compared with a dynamic threshold computed based on the weak signals generated by tissue backscattering. If the RF samples in the first third of the

segment are above the threshold, then the segment is assumed to satisfy the large amplitude feature, and hence the repetitive reflection pattern feature is verified. If the segment does not satisfy both features, the segment is ignored and the search for a segment that satisfies both features is continued.

The quantification of the repetitive reflection pattern feature is based on the spectral analysis presented in Subsection 2.B, in which the spectra of the signals reflected from a brachytherapy needle and a G17 needle are analyzed when both needles were embedded in water, separately filled with water and air, and imaged with the 4DC7-3/40 and MC9-4/12 transducers. This analysis indicated that the PSDs of the needle echoes possess a distinctive repetitive reflection pattern with a fundamental frequency between 0.40 and 0.75 MHz. In fact, the needle echoes received from the brachytherapy needle that was embedded in beef muscle and the four G17 needles that were inserted in porcine tissue specimens possessed fundamental frequencies within this range, as described in Subsections 4.B and 4.C, respectively. However, the use of this range of fundamental frequency to quantify the repetitive reflection pattern feature might not work if other types of needles are imaged or other probes with specifications different from the 4DC7-3/40 and MC9-4/12 transducers are employed. If other types of needles or transducers are employed, then the range of fundamental frequency should be recalculated based on experimental analysis similar to the analysis of PSDs of the needle echoes that was presented in Subsection 2.B.

The physical processes that are responsible for the repetitive needle reflection pattern can be investigated using models that describe ultrasound wave interaction with metal needles. The results reported in Table I suggest no correlation between the needle diameter and the values of Δf_1 and Δf_2 . The study by Zhu,³⁷ which modeled the bright comet tail of in-plane needles, suggested that ultrasound wave interaction with a metal needle might be interpreted using a metal plate reflection model of ultrasound waves. An interesting finding of this study is that the ultrasound signals reflected from a metal plate perpendicular to the incident ultrasound wave included a repetitive reflection pattern similar to the periodic reflection pattern of needle echoes that is reported in the present work. Another study by Mamou and Feleppa²⁸ observed a similar periodic repetitive pattern in the ultrasound signals received from brachytherapy seeds. In fact, this study indicated that the physical origin of the repetitive signals received from brachytherapy seeds is still under investigation. We hypothesize that there are factors that contribute to the repetitive needle reflection pattern, such as the multiple reflections within the needle and the interaction between the ultrasound wave and the metal needle shaft. A detailed model of ultrasound needle reflection is required to relate the repetitive needle reflection pattern to the metal structure of the needle as well as the acoustic properties of the metal needle shaft, the material inside the needle, and the medium surrounding the needle.

The estimation of the needle axis coordinates was performed by fitting the experimental arrival times of the needle echoes to the analytical arrival times described using Eq. (2). This equation assumes that the needle tip is not the minimizer of the orthogonal distance between the needle and the

transducer. This constraint can be addressed in future studies by analyzing the echoes reflected from the tip. In fact, such signature-based analysis of the echoes reflected from the needle tip can be used to extend the proposed method to enable accurate localization of the tip. Another assumption employed by the equation is that the tissue between the needle and the transducer is homogeneous and has a uniform sound speed. In real-life surgical procedures, the tissue between the transducer and the needle is usually composed of various structures that have different acoustic properties. In such procedures, the average sound speed of the tissue can be used to compute Eq. (2) and estimate the needle coordinates. This approximation is similar to the assumption employed in B-mode image formulation, in which the scanned tissue is assumed to be homogeneous with known sound speed.

An important assumption employed in the proposed needle detection method is that the needle is included in the imaging plane. However, if the needle is not included in the imaging, then the proposed method will correctly provide true negative identification of the needle. In fact, when the needle is not included in the imaging plane, then the echoes induced by other specular reflections will not meet in full the theoretical formula of needle echoes' arrival times described in Eq. (2) and will not completely satisfy the two needle-specific features used to estimate the experimental arrival times of needle echoes. Moreover, if some echoes are incorrectly identified as needle echoes, then there will be a significant difference between the theoretical and experimental arrival times of the incorrectly identified echoes, and hence the regression analysis employed to estimate the needle axis coordinates will be rejected based on the significant regression error.

The implementation of the proposed needle detection method requires access to the prebeamformed RF signals of the individual transducer elements. Such a requirement might not be supported in some ultrasound imaging systems. This limitation can be resolved by restricting the transmission and receiving of the circular wave to a small subaperture, called active transmit/receive subaperture, that forms a central axis orthogonal to the needle. The concept of the active transmit/receive subaperture is similar to the active receive aperture employed in this study. The number of elements in the active transmit/receive subaperture can be set to match the number of transmit/receive channels available in the imaging system so that the transmission and receiving operations are performed simultaneously on all elements of the subaperture.

In vivo application of the proposed method might be restricted to the two types of rigid needles examined in this study. Further studies are required to assess the capability of the proposed method to detect other types of needles. Moreover, the method can be extended to enable the localization of flexible needles by relaxing the assumption of the straight needle. Another challenge that limits clinical application of the proposed method is the relatively long processing time due to MATLAB implementation (processing time of ~3 min on Dell Vostro laptop with 2 GHz dual core processor and 3 GB memory). This limitation can be resolved by implementing the method on a parallel computing platform, such as GPU, using c++ language.

6. CONCLUSION

Estimating the needle axis coordinates in curvilinear ultrasound images has the potential to improve the outcome of various ultrasound-guided interventions, such as epidural anesthesia. In this study, a signature-based method was introduced to localize the needle axis in curvilinear ultrasound images. The method involves transmitting a circular ultrasound wave and analyzing the received signals to determine the arrival times of the needle echoes. The arrival times of needle echoes are used to estimate the needle axis coordinates based on the known needle reflection pattern of circular ultrasound waves. The method was used to estimate the axis coordinates of needles inserted in agar phantom, beef muscle, and porcine tissue specimens with maximum error rates on the order of 1 mm and 3° for the radial and azimuth coordinates, respectively. These results suggest that the accuracy and robustness of needle localization methods, such as needle segmentation algorithms, can be improved by incorporating the signature-based detection of the needle trajectory that is enabled using the proposed method.

ACKNOWLEDGMENTS

The authors thank Dr. Reza Zahiri-Azar for technical assistance with configuring the prebeamformed data acquisition (DAQ) system. This research is supported by the Natural Sciences and Engineering Research Council of Canada (NSERC) and the Canadian Institutes of Health Research (CIHR).

APPENDIX: THE MSAF TECHNIQUE

The MSAF technique presented in Ref. 31 was used with one-element active transmit aperture and 16-element active receive aperture ($K_r = 16$). In this technique, the active receive aperture during the firing of the i th element was composed of the elements in the range $[i - K_r/2, i + K_r/2]$. The image synthesized using MSAF can be expressed as³¹

$$I(r, \alpha) = \sum_n^{N-K_r} \sum_m^{K_r} s_{n,n+m}(r - \tau_{n,n+m}, \alpha), \quad (\text{A1})$$

where N is the number of transducer elements ($N = 128$), $s_{n,n+m}$ is the signal recorded by the $(m+n)$ th element during the actuation of the n th element, and $\tau_{n,n+m}$ is the beam-forming shift computed for the $n, n+m$ transmit, receive element combination. The MSAF image, $I(r, \alpha)$, was processed through envelope detection, scan conversion, and logarithmic compression to obtain a sector B-scan image.

^{a)}Electronic addresses: mohammad.aldaoud@giu.edu.jo, rohling@ece.ubc.ca, tims@ece.ubc.ca, and purang@ece.ubc.ca

¹R. Otto, J. Wellauer, G. Pedio, H. Burger, H. Eininghammer, R. Hauke, and T. Telger, *Ultrasound Guided Biopsy and Drainage* (Springer-Verlag, New York, NY, 1986).

²S. G. Shulman and D. E. March, "Ultrasound-guided breast interventions: Accuracy of biopsy techniques and applications in patient management," *Semin. Ultrasound, CT MRI* **27**, 298–307 (2006).

³D. Tran, A. Kamani, E. Al-Attas, V. Lessoway, S. Massey, and R. Rohling, "Single-operator real-time ultrasound guidance to aim and insert a lumbar epidural needle," *Can. J. Anesth.* **57**, 313–321 (2010).

- ⁴K. J. Chin, A. Perlas, V. W. S. Chan, and R. Brull, "Needle visualization in ultrasound-guided regional anesthesia: Challenges and solutions," *Reg. Anesth. Pain Med.* **33**, 532–544 (2008).
- ⁵G. A. Chapman, D. Johnson, and A. R. Bodenham, "Visualisation of needle position using ultrasonography," *Anaesthesia* **61**, 148–158 (2006).
- ⁶G. Reusz, P. Sarkany, J. Gal, and A. Csomos, "Needle-related ultrasound artifacts and their importance in anaesthetic practice," *Br. J. Anaesth.* **112**, 794–802 (2014).
- ⁷J. Huang, J. K. Friedman, N. V. Vasilyev, Y. Suematsu, R. O. Cleveland, and P. E. Dupont, "Imaging artifacts of medical instruments in ultrasound-guided interventions," *J. Ultrasound Med.* **26**, 1303–1322 (2007).
- ⁸K. J. Draper, C. C. Blake, L. Gowman, D. B. Downey, and A. Fenster, "An algorithm for automatic needle localization in ultrasound-guided breast biopsies," *Med. Phys.* **27**, 1971–1979 (2000).
- ⁹M. Ding and A. Fenster, "A real-time biopsy needle segmentation technique using Hough transform," *Med. Phys.* **30**, 2222–2233 (2003).
- ¹⁰S. H. Okazawa, R. Ebrahimi, J. Chuang, R. N. Rohling, and S. E. Salcudean, "Methods for segmenting curved needles in ultrasound images," *Med. Image Anal.* **10**, 330–342 (2006).
- ¹¹D. W. Cool, L. Gardi, C. Romagnoli, M. Saikaly, J. I. Izawa, and A. Fenster, "Temporal-based needle segmentation algorithm for transrectal ultrasound prostate biopsy procedures," *Med. Phys.* **37**, 1660–1673 (2010).
- ¹²P. M. Novotny, J. A. Stoll, N. V. Vasilyev, P. J. del Nido, P. E. Dupont, and R. D. Howe, "GPU based real-time instrument tracking with three dimensional ultrasound," *Med. Image Anal.* **11**, 458–464 (2007).
- ¹³M. Uhrcik, J. Kybic, H. Liebgott, and C. Cachard, "Model fitting using RANSAC for surgical tool localization in 3-d ultrasound images," *IEEE Trans. Biomed. Eng.* **57**, 1907–1916 (2010).
- ¹⁴M. Aboofazeli, P. Abolmaesumi, P. Mousavi, and G. Fichtinger, "A new scheme for curved needle segmentation in three-dimensional ultrasound images," in *Proceedings of The IEEE International Symposium on Biomedical Imaging: From Nano to Macro* (2009), pp. 1067–1070.
- ¹⁵M. Ding, H. N. Cardinal, and A. Fenster, "Automatic needle segmentation in three-dimensional ultrasound images using two orthogonal two-dimensional image projections," *Med. Phys.* **30**, 222–234 (2003).
- ¹⁶SonixGPS 0.55 mm Needle Sensor and Nerve Block Needle Kits User Manual, Ultrasonix Medical Corporation, 2011.
- ¹⁷J. Mung, F. Vignon, and A. Jain, "A non-disruptive technology for robust 3D tool tracking for ultrasound-guided interventions," in *Medical Image Computing and Computer-Assisted Intervention MICCAI 2011* (Springer, Berlin, 2011), Vol. 6891, pp. 153–160.
- ¹⁸H. Lu, J. Li, Q. Lu, S. Bharat, R. Erkamp, B. Chen, J. Drysdale, F. Vignon, and A. Jain, "A new sensor technology for 2D ultrasound-guided needle tracking," in *Medical Image Computing and Computer-Assisted Intervention MICCAI 2014* (Springer, Berlin, 2014), Vol. 8674, pp. 389–396.
- ¹⁹P. J. Stolka, P. Foroughi, M. Rendina, C. R. Weiss, G. D. Hager, and E. M. Boctor, "Needle guidance using handheld stereo vision and projection for ultrasound-based interventions," in *Medical Image Computing and Computer-Assisted Intervention MICCAI 2014* (Springer, Berlin, 2014), Vol. 8674, pp. 684–691.
- ²⁰S. M. Klein, M. P. Fronheiser, J. Reach, K. C. Nielsen, and S. W. Smith, "Piezoelectric vibrating needle and catheter for enhancing ultrasound-guided peripheral nerve blocks," *Anesth. Analg.* **105**, 1858–1860 (2007).
- ²¹J. D. Greer, T. K. Adebar, G. L. Hwang, and A. M. Okamura, "Real-time 3D curved needle segmentation using combined B-mode and power doppler ultrasound," in *Medical Image Computing and Computer-Assisted Intervention MICCAI 2014* (Springer, Berlin, 2014), Vol. 8674, pp. 381–388.
- ²²S. Cheung and R. Rohling, "Enhancement of needle visibility in ultrasound-guided percutaneous procedures," *Ultrasound Med. Biol.* **30**, 617–624 (2004).
- ²³B. C. H. Tsui, K. Doyle, K. Chu, J. Pillay, and D. Dillane, "Case series: Ultrasound-guided supraclavicular block using a curvilinear probe in 104 day-case hand surgery patients," *Can. J. Anesth.* **56**, 46–51 (2009).
- ²⁴D. S. Levi, "Intra-articular hip injections using ultrasound guidance: Accuracy using a linear array transducer," *PM&R* **5**, 129–134 (2013).
- ²⁵D. Souzdalnitski, I. Lerman, and T. M. Halaszynski, "How to improve needle visibility," in *Atlas of Ultrasound-Guided Procedures in Interventional Pain Management*, edited by S. N. Narouze (Springer, New York, NY, 2011), pp. 35–75.
- ²⁶M. I. Daoud, P. Abolmaesumi, W. You, S. E. Salcudean, and R. N. Rohling, "Signature-based algorithm for improved needle localization in ultrasound images: A feasibility study," in *Proceedings of The 2011 IEEE International Ultrasonics Symposium* (2011), pp. 1575–1578.
- ²⁷T. Saranteas and A. Karabinis, "Reverberation: Source of potential artifacts occurring during ultrasound-guided regional anesthesia," *Can. J. Anesth.* **56**, 174–175 (2009).
- ²⁸J. Mamou and E. J. Feleppa, "Singular spectrum analysis applied to ultrasonic detection and imaging of brachytherapy seeds," *J. Acoust. Soc. Am.* **121**, 1790–1801 (2007).
- ²⁹S. L. Marple, *Digital Spectral Analysis with Applications* (Prentice-Hall, Englewood Cliffs, NJ, 1987).
- ³⁰J. C. Lagarias, J. A. Reeds, M. H. Wright, and P. E. Wright, "Convergence properties of the Nelder-Mead simplex method in low dimensions," *SIAM J. Optim.* **9**, 112–147 (1998).
- ³¹M. Karaman, P.-C. Li, and M. O'Donnell, "Synthetic aperture imaging for small scale systems," *IEEE Trans. Ultrason., Ferroelectr., Freq. Control* **42**, 429–442 (1995).
- ³²A. Rasoulia, J. Lohser, M. Najafi, H. Rafii-Tari, D. Tran, A. A. Kamani, V. A. Lessoway, P. Abolmaesumi, and R. N. Rohling, "Utility of prepuncture ultrasound for localization of the thoracic epidural space," *Can. J. Anesth.* **58**, 815–823 (2011).
- ³³J. E. Browne, K. V. Ramnarine, A. J. Watson, and P. R. Hoskins, "Assessment of the acoustic properties of common tissue-mimicking test phantoms," *Ultrasound Med. Biol.* **29**, 1053–1060 (2003).
- ³⁴K. A. Topp and W. D. O'Brien, "Anisotropy of ultrasonic propagation and scattering properties in fresh rat skeletal muscle *in vitro*," *J. Acoust. Soc. Am.* **107**, 1027–1033 (2000).
- ³⁵S. A. Goss, R. L. Johnston, and F. Dunn, "Comprehensive compilation of empirical ultrasonic properties of mammalian tissues," *J. Acoust. Soc. Am.* **64**, 423–457 (1978).
- ³⁶SonixGPS for the SonixTouch Q+ Ultrasound System, Ultrasonix Medical Corporation, Richmond, BC, Canada, 2014.
- ³⁷M. Zhu, "Real-time B-mode ultrasound image simulation and artifacts modelling of needles and brachytherapy seeds," Master's thesis, University of British Columbia, 2009.